Nonlinear growth of swell by wind under cross sea

Takehiko Nose [a] Takuji Waseda, [a] Keita Nishizawa,[b] Tsubasa Kodaira, [a] Yasushi Fujiwara, [c]
Alberto Alberello, [d]

[a] *Department of Ocean Technology Policy and Environment,*
Graduate School of Frontier Sciences, The University of Tokyo
[b] *Monohakobi Technology Institute*
[c] *Kobe University*
[d] *School of Engineering, Mathematics and Physics, University of East Anglia*

Corresponding author: Takehiko Nose, tak.nose@edu.k.u-tokyo.ac.jp

Early Online Release: This preliminary version has been accepted for publication in *Journal of Physical Oceanography*, may be fully cited, and has been assigned DOI 10.1175/JPO-D-24-0251.1. The final typeset copyedited article will replace the EOR at the above DOI when it is published.

ABSTRACT: The development of swell under a cross sea was investigated because four drifting wave buoys in the marginal ice zone near the Chukchi Sea measured a wave event contrary to the waves expected following the fetch law. The expected sea state at the ice edge under southeasterly winds of 10–15 ms^{-1} was 2–3 m waves with a 6–7 s period from the southeast. However, the dominant buoy-measured wave was almost 90 degrees off the wind from the southwest with 2 m wave height and 9 s period. Since the phase speed was 14 ms^{-1} and the oblique wind speed was 10-15 ms^{-1}, the wave age of the measured waves was >> 1. A hindcast model using the discrete interaction approximation (DIA) method, surprisingly, reproduced the buoy-measured swell including the direction. An analysis of the source terms revealed that the swell evolved over hundreds of kilometers across the ice-free ocean, and central to the swell development was the nonlinear coupling of wind energy input and the swell spectral peak via the nonlinear interactions source term. The implications of using the DIA were evaluated through idealized cross-sea simulations using the EXACT-NL model. The EXACT-NL simulations were qualitatively consistent with the DIA results and corroborated the hindcast finding. Moreover, the EXACT-NL simulations provided additional insights into the mechanisms of nonlinear energy transfer, which were found to align with the Masson (1993) theory of nonlinear coupling between swell and wind waves.

SIGNIFICANCE STATEMENT: Realistic formulations of physical processes occurring near the ocean surface are essential for the accuracy of ocean wave forecasts that we use for a wide range of recreational and engineering applications. To evaluate whether a model can reproduce complex sea conditions, validation against observations is important. We investigated a complex cross-sea condition using drifting wave buoy observations and wave model results and revealed a mechanism that allowed swell waves to grow over hundreds of kilometers when the wind was blowing from oblique directions. The cross sea is a well-known hazard for shipping, and our study presented a new insight into the swell evolution under a cross sea.

1. Introduction

Ocean waves grow due to the effect of wind stress over the ocean surface (Jones and Toba 2001). Idealized wind wave growth can be estimated based on the fetch law also known as Kitaigorodskii's scaling. The core assumption here is the wind waves develop under steady wind from a straight shoreline. The non-dimensional energy $\epsilon = \sigma^2 g^2 / U^4$ and frequency $\nu = f_p U / g$ are a function of the non-dimensional fetch $\chi = xg/U^2$. σ is the surface elevation variance, f_p is the peak frequency of a wave spectrum, x is the fetch distance, g is the gravitational acceleration, and U is the wind speed. $\epsilon = f(\chi)$ and $\nu = f(\chi)$ can be used to estimate sea states under various idealized growth cases.

When we deployed drifting wave buoys in the marginal ice zone (MIZ) during the 2020 Arctic Ocean expedition by R/V Mirai[1], a wave event was observed that was contrary to the waves expected following the typical fetch growth. When moderate to strong southeasterly winds of 10–15 ms^{-1} developed over the ice-free ocean (as depicted in a series of wind fields in Figure 1), estimated wind waves at the ice edge along the wind direction would be approximately 2–3 m significant wave height and 6–7 s peak period adopting the Donelan et al. (1985) scaling of the fetch law over the 300 km distance. The drifting wave buoys in the MIZ, however, measured swell with a significant wave height of 2 m and a peak period of 9 s with a direction from the southwest: the wave age was >> 1, and this swell was contrary to the expected waves following the fetch law. The wave age here was calculated as $\frac{C_p}{Ucos(\theta-\phi)}$ where C_p is the wave phase speed, and θ and ϕ are the wave and wind directions, respectively. After contemplating various scenarios of wave origin including the slanting fetch effect (Donelan et al. 1985; Walsh et al. 1989; Ardhuin et al. 2007; Pettersson

[1] https://www.jamstec.go.jp/iace/e/report/pdf/2020.MR20-05.pdf

Accepted for publication in *Journal of Physical Oceanography*. DOI 10.1175/JPO-D-24-0251.1.

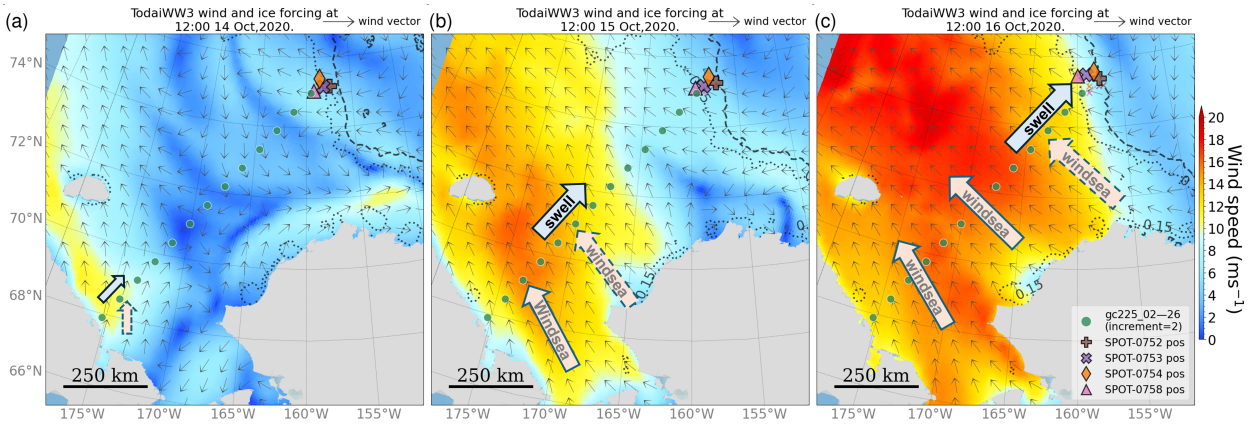

FIG. 1: The wind (color) and ice (contours) conditions (from the hindcast model) at 12:00 on (a) 14 Oct, (b) 15 Oct, and (c) 16 Oct during which the southwesterly swell evolved. The wave buoy trajectories and their positions are also shown in dotted lines and markers. The great circle path with 225-degree heading from the Spotters at 80 km spacing is shown in green markers. The figure is also annotated with wind-sea and swell arrows. The dotted-wind-sea outlines depict wind-sea inhibition (as will be discussed in Sections 5*b* and 6) and the swell arrow length is scaled to the cross-sea region, i.e., the region of swell presence, estimated from Figure 5 (described in Section 4*b*).

et al. 2010; Tamura et al. 2021), we were unable to explain how the measured swell developed using only the buoy data. As such, we conducted a wave hindcast of the swell event for further insights. The hindcast model, surprisingly, reproduced bulk statistics including the wave direction; swell tracking of the modeled directional spectra revealed that southwesterly energy first appeared near coastal waters of the Siberian coast, located hundreds of kilometers away from the buoys. These waves somehow evolved as southwesterly swell (referred to herein as "crossing swell") and propagated to the MIZ drifting buoys located north of the Chukchi Sea.

The hindcast was conducted using a third-generation spectral wave model, WAVEWATCH III. The wave evolution in time and space $S(f,\theta)$ is described (neglecting currents) by a differential equation

$$\frac{\partial N}{\partial t} + \nabla \cdot \vec{c} N = s_{\text{in}} + s_{\text{ds}} + s_{\text{nl}}, \tag{1}$$

where N is the action density spectrum and $\vec{c}$ is the wave propagation in time and space. f denotes frequency and θ is the wave direction. The cornerstone of the third-generation spectral wave model is the explicit treatment of the nonlinear interactions source term s_{nl}. The well-known Hasselmann (1962) expression describing the net energy transfer within the action density spectrum at $\mathbf{k}_4$ due

Accepted for publication in *Journal of Physical Oceanography*. DOI 10.1175/JPO-D-24-0251.1.

to all quadruplet interactions involving $\mathbf{k}_4$ is

$$\frac{\partial N(\mathbf{k}_4)}{\partial t} = \iiint G\delta(\mathbf{k}_1+\mathbf{k}_2-\mathbf{k}_3-\mathbf{k}_4)\delta(\omega_1+\omega_2-\omega_3-\omega_4) \tag{2}$$

$$\times [N_1N_2(N_3+N_4) - N_3n_4(N_1+N_2)]\, d\mathbf{k}_1 d\mathbf{k}_2 d\mathbf{k}_3.$$

Here, ω and k are the radian frequency and wavenumber, G is a coupling coefficient, and the delta functions ensure nonlinear interactions only occur for the quadruplets satisfying the exact resonant conditions therein. Nonlinear interactions play an important role in the wind-wave spectral energy balance, and their implementation in spectral wave models has enhanced the predictability of ocean wave forecasts. Numerical computation of the nonlinear interactions is based on the symmetric integration technique of the Hasselmann integral (Hasselmann and Hasselmann 1985), which is suitable for modeling idealized cases (e.g., Young et al. (1987); Young and Van Vledder (1993); van Vledder and Holthuijsen (1993)), and parameterizations developed from the idealized cases. For the latter, a parameterization known as the discrete interaction approximation (DIA) method (Hasselmann et al. 1985) is computationally efficient for large-scale models, and thus often adopted in operational wave models.

Directional responses of two wave systems and the role of s_{nl} were investigated by Young et al. (1987); van Vledder and Holthuijsen (1993) in the context of a sudden wind shift for duration-limited wave growth: $\frac{\partial N}{\partial t} = s_{\mathrm{tot}}$. The total source term s_{tot} is the summation of the wind energy input s_{in}, the energy dissipation term s_{ds}, and s_{nl}. While van Vledder and Holthuijsen (1993) used only the EXACT-NL model, Young et al. (1987) used both the EXACT-NL and DIA models and evaluated the directional responses for both models. Young et al. (1987) simulated wind shift angles from 30 to 150 degrees at 30-degree increments. For wind shift angles of 30 and 60 degrees, they found the wind sea rotates to the new wind direction via the s_{nl} coupling of the wind input peak and the existing spectral peak. At wind shift angles of 90 degrees and more, a secondary peak in the new wind direction developed as the coupling between the wind input energy and the existing spectral peak becomes weak, and the old spectral peak decays slowly. van Vledder and Holthuijsen (1993) investigated sudden wind shifts of 30 and 90 degrees, and they found that a new wind-sea peak appeared for both cases. The old existing and new secondary peaks merged quickly for 30 degrees while the peaks for the 90-degree case remained separated and the old spectral

Accepted for publication in *Journal of Physical Oceanography*. DOI 10.1175/JPO-D-24-0251.1.

peak dissipated in time. In contrast to Young et al. (1987), van Vledder and Holthuijsen (1993) attributed the merging of the peaks to the effect of s_{in}, that wind input region was directionally spread over the old spectral peak for the 30-degree wind shift.

The shape of the positive part of s_{nl} for a 90-degree wind shift (Figure 8 of van Vledder and Holthuijsen (1993)) is directionally spread over 90 degrees, which is interesting because Young et al. (1987) found that the s_{nl} coupling of old and new peaks for wind shifts larger than 60 degrees was weak. The s_{nl} shape of van Vledder and Holthuijsen (1993) is a mechanism that redistributes energy from the oblique wind input to the old spectral peak at relatively large angles. Steering of the peak wave direction obliquely to the wind due to wave-wave nonlinear interactions under slanting fetch was also described in Pettersson et al. (2010) for a narrow bay and Ardhuin et al. (2007) for a coastal area, although the interactions between wind and waves for their studies occurred for wind-sea conditions (i.e., wave age $< 1.$). There is also a theory that describes the transfer of wind-sea energy to swell. Masson (1993) studied swell decay under a bimodal wind-wave and swell sea state, in which the swell spectrum was assumed to be very narrow (a delta function) with a stationary wind-sea spectrum. When the swell spectral peak is just below the wind-sea peak frequency, there is a region in the frequency-direction space where there is a negative swell decay rate; nonlinear coupling between swell and wind sea causes swell to grow at the expense of the wind sea. Masson (1993) estimated the peak swell growth occurs when the wind-sea and swell directions are 35 degrees oblique to each other. Tamura et al. (2009) showed evidence of the Masson (1993) theory at work in the Pacific Ocean under rapidly increasing winds during a cold front passage event.

Because of the model and observation agreement during the measured wave event (as described in Section 3*b*), the hindcast model was considered to be a tool to investigate the southwesterly crossing swell evolution along its propagation path. The use of the DIA parameterization for s_{nl} is a notable contrast to the exact computations used in the literature discussed above. Accordingly, the implications of using the DIA method was evaluated against the full Boltzmann computation of Eq. 2, known as the EXACT-NL model, in idealized cross-sea scenarios, which will be thoroughly discussed in Section 6.

Accepted for publication in *Journal of Physical Oceanography*. DOI 10.1175/JPO-D-24-0251.1.

2. Methods

a. Wave buoy observation

Wave observations were made using Sofar Ocean's Spotter buoys. They were deployed from R/V Mirai during the MR20-05C Arctic Ocean expedition in October 2020. The Spotter buoy measures waves based on the ocean surface displacements with a vertical displacement accuracy of around ±2 cm. The details of wave statistics that are obtained from a Spotter are provided in Sofar Ocean's technical reference manual[2]. Significant wave heights H_s and peak periods T_p were estimated from the surface elevation variance density spectrum $S(f)$. Instead of Sofar's mean period, we used -1-moment period, which was calculated as $T_{0m1} = m_{-1}/m_0$. Directional information including spreading was estimated using the directional moments.

Four Spotter buoys, named SPOT-0752, SPOT-0753, SPOT-0754, and SPOT-0758 were deployed between 00:58 and 06:58 on 13 Oct spread over a distance of approximately 50 km from the ice edge near 114° W, 75° N (the buoy locations and ice edge are shown in Figure 1). We also deployed another Spotter buoy named SPOT-0759 in the open water at 19:27 on 17 Oct. The aim was to measure open-water wave conditions adjacent to the ice edge; we planned to deploy it just before the predicted wave event, but it was deployed after the storm when the sea state became calm enough for the R/V Mirai crew to safely deploy the buoy. Although it missed the storm peak, the SPOT-0759 buoy data were still included in this study.

b. Spectral wave model

The origin of the measured southwesterly swell was not easily identified from the synoptic condition (as the ice-free ocean wind directions were southeasterly); as such, spectral wave modeling of the Arctic Ocean was conducted to gain insights into the buoy-measured waves. The spectral wave model used for this study was based on the WAVEWATCH III wave model that has been developed under the community modeling framework (WW3DG 2019); we will label our wave model as TodaiWW3-ArCS from herein. TodaiWW3-ArCS has been developed and used to provide short-range wave forecasts to support the annual Arctic Ocean expedition by R/V Mirai, which usually takes place sometime between Aug and Oct. The forecast model setup, such as spatial resolutions, was determined to meet the forecast time constraints, and this setup was adopted for the hindcast.

[2]https://content.sofarocean.com/hubfs/Spotter%20product%20documentation%20page/Sofar%20-%20Technical_Reference_Manual.pdf

Accepted for publication in *Journal of Physical Oceanography*. DOI 10.1175/JPO-D-24-0251.1.

TodaiWW3-ArCS adopts a nested system in which the large-scale model covers the pan-Arctic domain with a 16-km horizontal resolution, and a nested model covers the R/V Mirai planned track at a finer 8-km horizontal resolution. The large-scale model was previously introduced in the Nose et al. (2018) study. The spectral grid was configured with 36 directional and 35 frequency bins with the latter ranging from 0.041 to 1.052 Hz. The spatial grid was based on the curvilinear grid implemented by Rogers and Campbell (2009) with a polar stereographic projection of 75° N latitude (produced by Mathworks Matlab's polarstereo_inv function). The geographical grid was defined using the International Bathymetry Chart of the Arctic Ocean (Jakobsson et al. 2012) and the Global Self-consistent, Hierarchical, High-resolution Geography shoreline data (Wessel and Smith 1996). The nested model corner points are as follows: upper right; −112.7510° W, 77.7974° N, upper left; 158.9625° E, 84.9287° N, lower right; −154.9073° W, 63.8152° N, and lower left; 175.6807° E, 66.1494° N.

TodaiWW3-ArCS included additional source terms, so the right-hand side of (1) is

$$s_{\mathrm{tot}} = (1 - c_i)(s_{\mathrm{in}} + s_{\mathrm{ds}}) + c_i s_{\mathrm{ice}} + s_{\mathrm{nl}} + s_{\mathrm{bot}}, \tag{3}$$

in which relative contributions of the physical processes are scaled by the sea ice concentration c_i. We are aware that Herman and Bradtke (2024); Herman (2024) revealed limitations of the default scaling to reproduce sea states in frazil ice under severe winds; since the core of our analysis took place in the ice-free water, the study outcome is unlikely to be affected by the c_i scaling issues or the c_i uncertainty, e.g., Nose et al. (2020). To simulate the physical processes of the ocean waves, various physics packages for the respective source terms are available within the WAVEWATCH III source codes (WW3DG 2019). For the essential wind energy input s_{in} and wave dissipation s_{ds} source terms, we selected the so-called "ST6" physics parameterizations (Rogers et al. 2012; Zieger et al. 2015; Liu et al. 2019); "ST6" was also selected in our previous Arctic Ocean modeling study in Nose et al. (2020). The DIA method labeled as "NL1" in the name list was selected for the nonlinear interactions source term. Wave dissipation due to seabed is necessary for water depths relevant to the wavelength length scale, which was the case over a shoal along the crossing swell path: here, we used the JONSWAP package "BT1" (Hasselmann et al. 1973) for s_{bot}. Finally, wave-ice interaction parameterization was needed because the drifting buoys were located in the MIZ. Because of the heterogeneity of the ice conditions, we consider the viscoelastic model of

Accepted for publication in *Journal of Physical Oceanography*. DOI 10.1175/JPO-D-24-0251.1.

Wang and Shen (2010) labeled as "IC3" in the WAVEWATCH III framework to be practical in the MIZ. This modeling approach was developed to simulate the aggregated effect of wave attenuation due to sea ice including the attenuation within the ice layer for example.

The surface and lateral boundary conditions were as follows. The ECMWF Reanalysis (ERA5) 10 m surface winds (Hersbach et al. 2023) were used for the wind forcing, and the Regional Ice-Ocean Prediction System (RIOPS) (Smith et al. 2021) produced by Environment and Climate Change Canada was used for the ice forcing. The wind forcing has a spatial resolution of 0.25 degrees. The RIOPS ice forcing formed the lateral boundary condition and included sea ice concentration and thickness, which is produced at the spatial resolution of nominal $1/12^{th}$ degrees. For the RIOPS ice forcing, 0–23 hour lead time forecasts were collated during the simulation period.

The same wave statistics as described in the preceding subsection *a* were produced at each model grid point with a temporal resolution of 3-hour intervals. We also output the wave directional spectra and source terms along the southwesterly swell ray. The output points were produced at 40-km spatial intervals along the southwesterly great circle path from the SPOT-0752 position (shown as green markers in Figure 1).

3. Results

a. Wave buoy observations

The wave statistics and wind conditions at the buoy locations are presented in Figure 2a. The Spotter buoys' wave statistics shown in Figure 2b indicate calm seas, i.e,. H_s less than 1 m, until 16 Oct; in the ice-free ocean, however, moderate–strong southeasterly wind conditions developed in the Russian Arctic as a low-pressure system moving northward from Siberia was blocked by high-pressure system over the central Arctic Ocean, generating sustained southeasterly winds of 10–15 ms^{-1} in the Chukchi and East Siberian seas from late 14 Oct (see the wind fields in Figure 1). The H_s in the adjacent ice-free ocean exceeded 4 m based on the hindcast model results.

The Spotter buoys began detecting the arrival of swell energy on 16 Oct, and SPOT-0752, located farthest from the ice edge, measured 0.5 m H_s while SPOT-0758 located closest to the ice edge measured H_s up to 2 m. The mean and peak wave periods during this wave event (from 06:00 16 Oct) was around 9 s. The -1-moment wave period for SPOT-0758 was lower; the T_{0m1} wave periods below 6 s just before the swell arrived indicates that wind sea was measured by SPOT-0758.

Accepted for publication in *Journal of Physical Oceanography*. DOI 10.1175/JPO-D-24-0251.1.

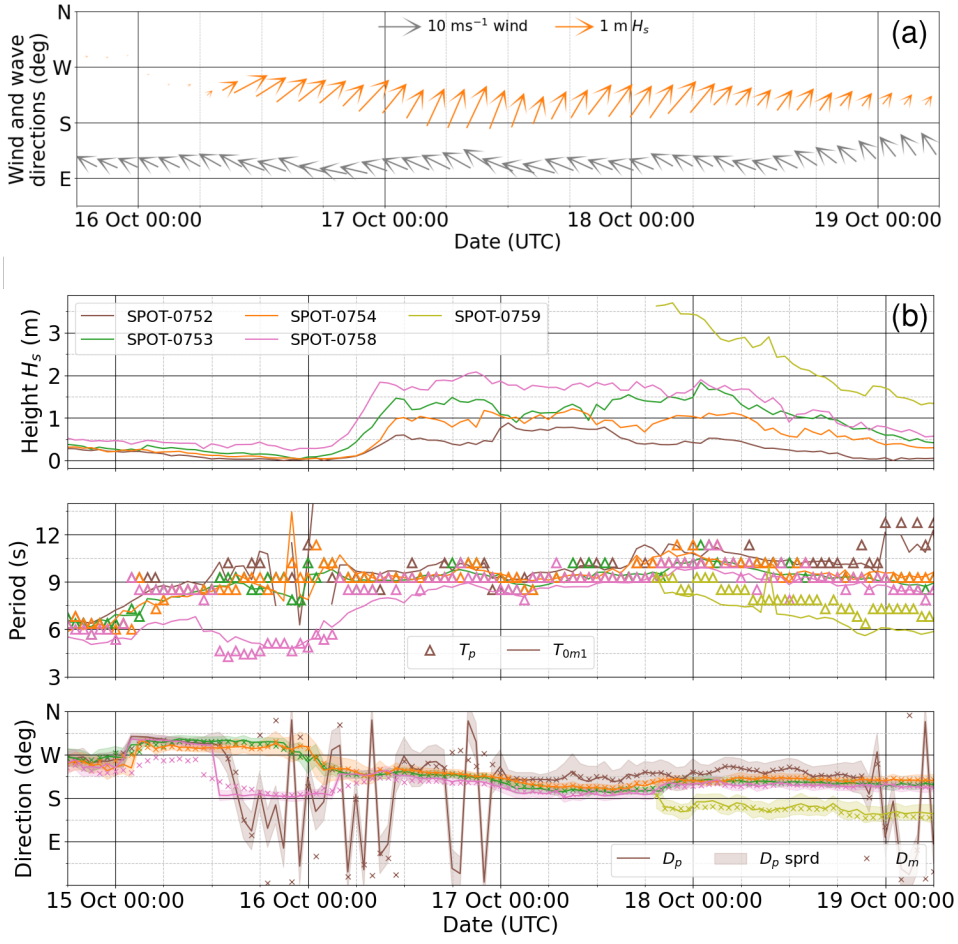

FIG. 2: (a) Time series of Spotter measured peak wave directional vectors scaled by wave height H_s, and ERA5 wind vectors at SPOT-0754 positions between 16 and 18 Oct. (b) Time series of Spotter measured wave heights, periods, directions by the Spotter wave buoys between 15 and 18 Oct (bottom panel).

Wave directions were primarily southwest, but with a slight tendency to shift more west farther into the ice cover, which is analogous to the numerical evidence that the direction turns orthogonal to the ice edge (Alberello et al. 2024). Peak wave directions D_p and their spreading, and mean wave directions D_m are shown in the bottom panel of Figure 2b. Since D_p and D_m have similar values, we can interpret that the buoys' directional spreading was small, i.e., waves were mostly coming from one direction. Note that the SPOT-0752 wave directions were noisy until 17 Oct, so we need to extrapolate the wave directions from the down-wave buoys and assume they were also primarily from the southwest. Around 00:00 on 17 Oct, there is a jump in the SPOT-0752 H_s; the wave directions for all buoys also veered towards southerly directions with the buoys closer to the

Accepted for publication in *Journal of Physical Oceanography*. DOI 10.1175/JPO-D-24-0251.1.

ice edge showing more southerly tendency. Perhaps waves from a different origin arrived at the buoy locations at this time, implying the dominant southwesterly waves were observed mostly on 16 Oct by the buoys.

Peak wave directional vectors and the ERA5 wind vectors at the SPOT-0754 buoy position are depicted in Figure 2a. The data clearly show that waves were coming from different directions to that of the wind. Moreover, the wave age was well over one, and as such, we interpreted the crossing swell was likely generated at and arrived from the far field sea.

b. Hindcast validation against the buoy observations

Hindcast wave statistics were compared with the Spotter data between 15 and 18 Oct 2020. The time series plots as shown in Figure 3 depict qualitative model-observation agreements for wave heights, periods, and wave directions especially once the swell arrived on 16 Oct. Notable discrepancies are a slight underestimation of mean wave period T_{0m1} for SPOT-0753 and -0754 on 15 Oct, while the model seemingly could not capture the measured wind sea for SPOT-0758 before the swell arrived on 16 Oct (the model did not reproduce the buoy measured T_{0m1} and D_m). These discrepancies imply that TodaiWW3-ArCS was unable to reproduce the wind-sea conditions in or near the ice cover, which could be due to the c_i scaling limitations of the wind energy input source term s_{in} as described in Herman (2024). Regarding SPOT-0752, the model T_{0m1} was generally underestimated and the jump in H_s around 00:00 on 17 Oct was also not reproduced. Wave heights deviated for SPOT-0753,-0758, and -0759 on 18 Oct as the wave energy tapered off. The mean wave directions also differed for SPOT-0752 until 12:00 on 16 Oct, but this is likely because of the observational error. Time series comparing the peak wave period and directions T_p and D_p for TodaiWW3-ArCS and Spotter data, which showed analogous trends, are provided in Appendix A for reference.

Despite these model deviations at the detailed level, it seems reasonable to interpret that the TodaiWW3-ArCS hindcast qualitatively simulated the general features of the swell propagation in the ice-free ocean and into the MIZ; the buoy measured southwesterly swell at the MIZ was likely a realistic condition. Therefore, TodaiWW3-ArCS source term outputs were used as a tool to investigate the onset of the crossing swell and how the it evolved before arriving at the Spotter buoys in the MIZ.

Accepted for publication in *Journal of Physical Oceanography*. DOI 10.1175/JPO-D-24-0251.1.

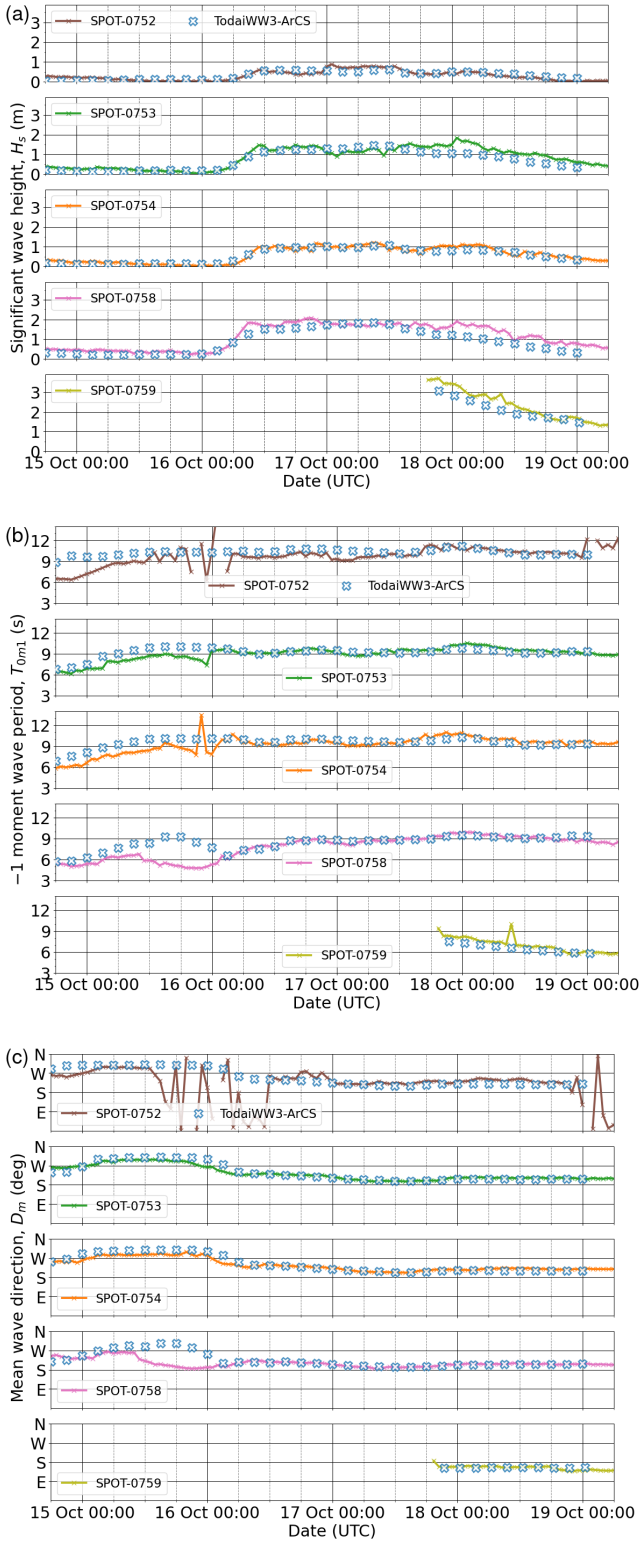

FIG. 3: Comparison of TodaiWW3-ArCS and Spotter buoy wave statistics during the wave event: (a) significant wave height H_s, (b) mean wave period T_{0m1}, and (c) mean wave direction D_m.

Accepted for publication in *Journal of Physical Oceanography*. DOI 10.1175/JPO-D-24-0251.1.

4. Analysis of crossing swell

a. Wind field and the wave generation

As introduced in Section 1, the wind field (speed and normalized vectors of the TodaiWW3-ArCS forcing) at 12:00 on (a) 14 Oct, (b) 15 Oct, and (c) 16 Oct over the Chukchi and East Siberian seas are shown in Figure 1. The panels show the development of moderate–strong southeasterly winds over the ice-free ocean from a calm condition. The southeasterly winds first grew as turning winds between 12:00 on14 Oct and 12:00 on 15 Oct near the Siberian coast. The southeasterly winds gradually migrated northward and the southeast became the dominant wind condition in the ice-free ocean (e.g., Figure 1c).

Swell tracking was conducted to identify the origin of the swell. TodaiWW3-ArCS was unable to utilize the WAVEWATCH III wave system tracking output because it uses a non-regular geographical grid (i.e., swell tracking output is only available for regular grid); as such, we manually traced the crossing swell by inspecting directional spectra along the great circle path with 225 degrees heading from the SPOT-0752 position on 16 Oct (referred to as the gc225 path herein), which extended to around 1,000 km at the Siberian coast (the bearing at the Siberian coast is about 210 degrees because the path is geodesic). If we were to assume the swell origin was as far away as the Siberian coast, we estimated that the crossing swell developed sometime in the second half of 14 Oct (taking c_g of 9 s wave as ≈25 km/hr). Indeed, the directional spectrum at gc225_24 on 12:00 14 Oct was the first sign of southwesterly energy that appeared along the gc225 path in TodaiWW3-ArCS. As the moderate winds were developing at 12:00 on 14 Oct, there was a time when the wind was from the south but with a slight west to it. During this time, energy was distributed symmetrically about the wind direction via the wind input s_{in} and nonlinear interactions s_{nl} source terms including some energy into the southwest sector (see s_{nl} in Figure 4a). The frequency-directional spectrum at gc225_24 for 12:00 on 14 Oct was the initial energy being generated in the southwesterly directions and shown in Appendix B. The s_{nl} directional features shown in Figure 4a reflect the spectral energy balance as described in Young and Van Vledder (1993); energy from the $\frac{f}{f_p} > 1$ frequency region is redistributed to the $\frac{f}{f_p} \leq 1$ space. Nonlinear interactions tend to directionally broaden the energy in the former region while the $\frac{f}{f_p} \leq 1$ space in the spectrum is narrower (but still spread over 90 degrees).

Accepted for publication in *Journal of Physical Oceanography*. DOI 10.1175/JPO-D-24-0251.1.

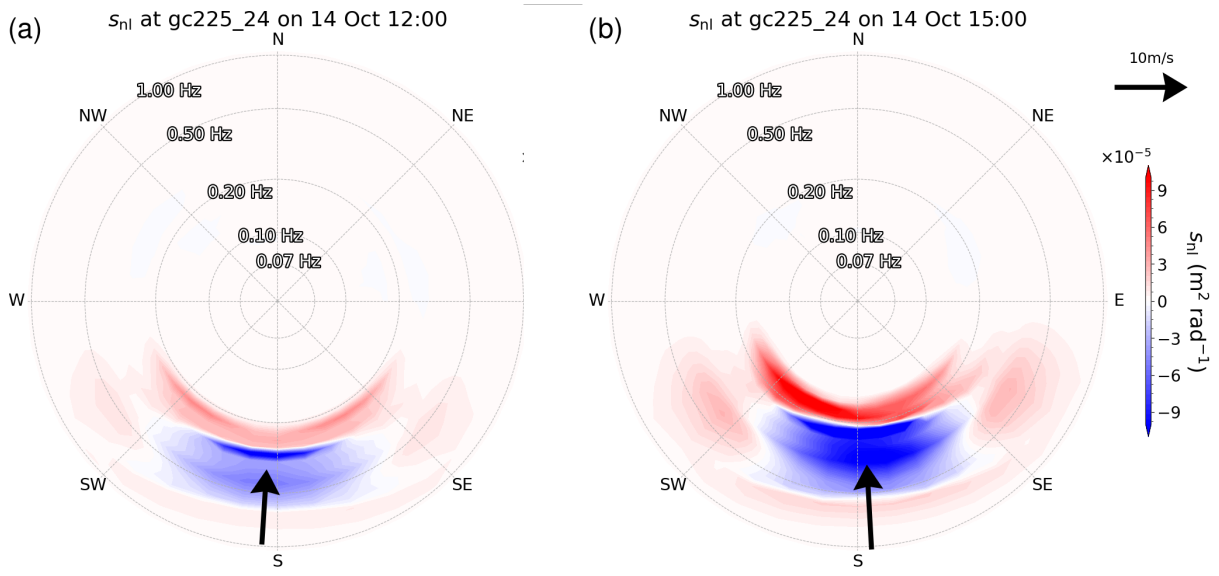

FIG. 4: Nonlinear interactions source term s_{nl} is shown at the gc225_24 position when the southwesterly energy first appeared at (a) 12:00 and (b) 15:00 on 14 Oct. The black arrows indicate the wind vector.

By 15:00, the wind was still southerly but shifted slightly to the east. At this time, the nonlinear interactions source term became skewed; the energy being spread from $\frac{f}{f_p} > 1$ to $\frac{f}{f_p} \leq 1$ was no longer symmetrical to the wind input direction as shown in Figure 4b. The nonlinear interactions redistributed more energy to the southwest and south-southwest space rather than to the $\frac{f}{f_p} \leq 1$ space aligned with the wind direction. In other words, energy from the wind input direction was taken away to the spectral peak in the previous wind direction. After this time, we can track the southwesterly energy along the gc225 path (as described in the following subsection *b*).

b. Crossing swell propagation

Figure 5 shows the directionally discretized wave energy $S^*(f)$ between 202.5–247.5 degrees ($\int_{202.5}^{247.5} S(f,\theta)d\theta$) along the gc225 path. The x-axis represents distances, i.e., 26 spectra at the model output points, but also the spectral frequencies within each grid. The y-axis is spectral density, but each line interval also represents the time of 3 hours. The figure shows wave energy evolution in time and space; the wave energy propagated from generation near the Siberian coast and traveled to the MIZ north of the Chukchi Sea.

The evolution of the southwesterly wave energy from 14 to 16 Oct along the gc225 path is clear. After the onset of the crossing swell, southwesterly energy continued for several hours.

Accepted for publication in *Journal of Physical Oceanography*. DOI 10.1175/JPO-D-24-0251.1.

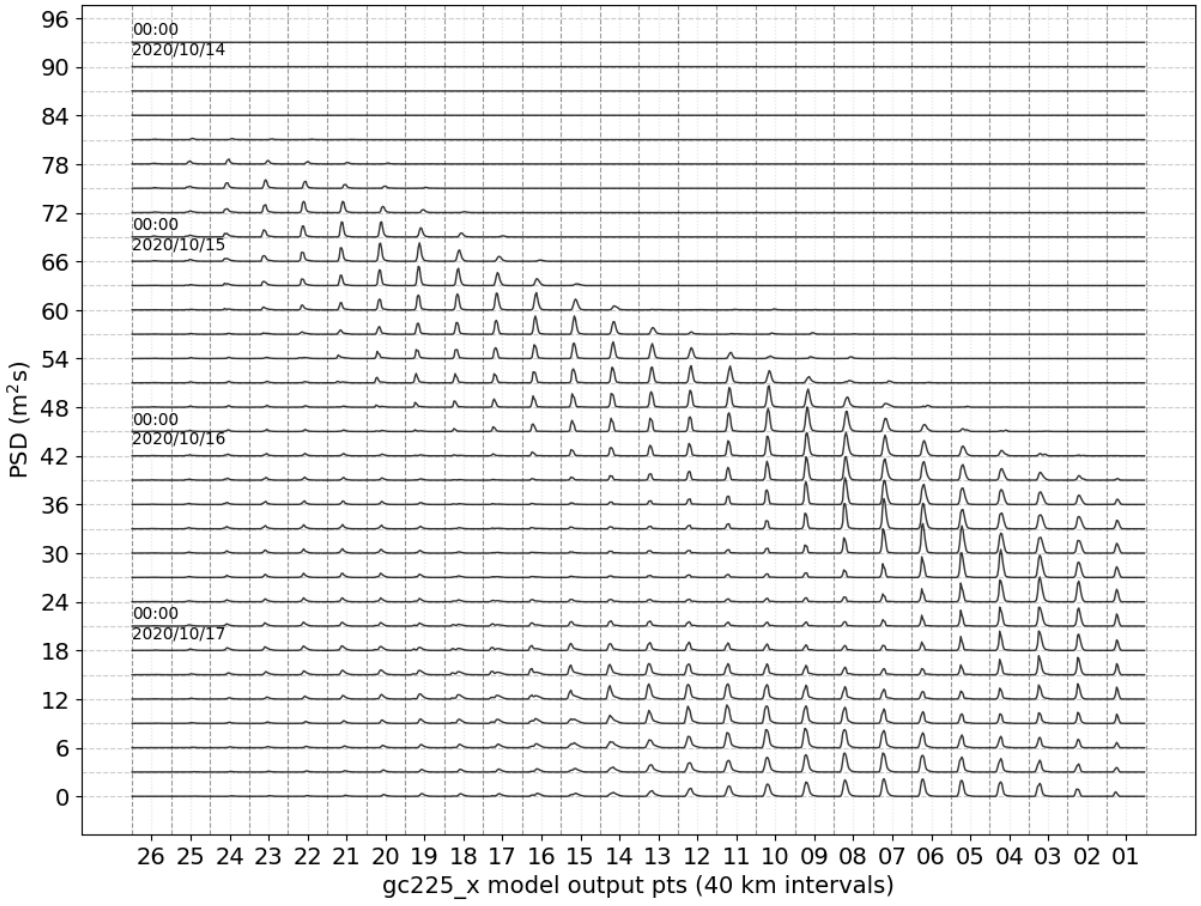

FIG. 5: Crossing swell evolution based on the southwesterly discretized power spectral density (i.e., $S^*(f) = \int_{202.5}^{247.5} S(f,\theta)d\theta$) along the gc225 points between 14 and 17 Oct. The x-axis represents distances with 40 km spacing between adjacent points, and within each grid, it is also spectral frequencies. The y-axis is variance density, but each horizontal line represents time of 3-hourly intervals.

These waves initially grew for approximately 200 km. The southwesterly waves stopped growing and partially dissipated over a shallow shoal at gc225_18. The remained wave energy continued to propagate, but the growth stagnated. By late 15 and on 16 Oct, the winds over the ice-free ocean strengthened to 10–15 ms^{-1} (see Figure 1); the southwesterly waves appeared to regrow near gc225_12. The waves eventually propagated to the MIZ where the waves attenuated due to the ice-to-wave effects. The swell presence relative to the wind field is also illustrated in Figure 1.

The propagation of the crossing southwesterly waves is intriguing because these waves continued to propagate hundreds of kilometers without experiencing southwesterly winds after its generation

Accepted for publication in *Journal of Physical Oceanography*. DOI 10.1175/JPO-D-24-0251.1.

(i.e., the winds were from the wrong direction). The evolution of the crossing swell directional spectra is described in the following subsection.

c. The evolution of crossing swell directional spectra

The directional wave spectra were tracked from generation to approaching the MIZ. The swell was manually tracked by assuming the following wave propagation speed approximations based on the spectral peak energy.

- Between gc225_24 and 20, we take the group speed c_g of 5 s wave period to be ≈4.0 ms^{-1}, which travels roughly 40 km in 3 hours (i.e., 1 gc225 interval in 3 hours).
- Between gc225_20 and 08, we take the c_g of 7 s wave period to be ≈5.5 ms^{-1}, which travels roughly 120 km in 6 hours (i.e., 2 gc225 intervals in 6 hours).
- From gc225_08 onward, we take the c_g of 9 s wave period to be ≈7.0 ms^{-1}, which travels roughly 75 km in 3 hours (i.e., 2 gc225 intervals in 3 hours).

A series of directional spectra were extracted based on the above traveling speeds and shown in Figure 6. The respective wind vector was also shown in each directional spectrum. Consistent with the energy propagation shown in Figure 5, the propagation of the southwesterly energy is apparent. The spectra also show that the crossing swell evolved without direct input from the winds after the generation.

Figure 6a is a directional spectrum 6 hours after the generation. A directionally broad spectral peak was spread in the space between south and southwest directions, while the wind was obliquely blowing at roughly 45 degrees off the main wave direction. By b, the southwesterly energy grew despite the wind becoming more southeast, and the peak energy shifted more southwesterly. The directional spread was larger with energy spread between the southwest and southeast sectors. Figure 6c is a directional spectrum at gc225_17, which is near a shoal, and the reduction in energy is apparent (energy dissipation in the s_{bot} was confirmed at gc225_18, not shown here). By the time the crossing swell reached gc225_14 and _11, at 12:00 and 18:00 on 15 Oct, southeasterly winds strengthened as shown in d and e. By this time, the re-growth of the crossing swell peak is also apparent. Interestingly, the directional spectrum was unimodal in Figure 6f in the crossing swell direction, and the wind speed was noticeably lower; the magnitude of s_{in}, s_{ds}, and s_{nl} source terms

Accepted for publication in *Journal of Physical Oceanography*. DOI 10.1175/JPO-D-24-0251.1.

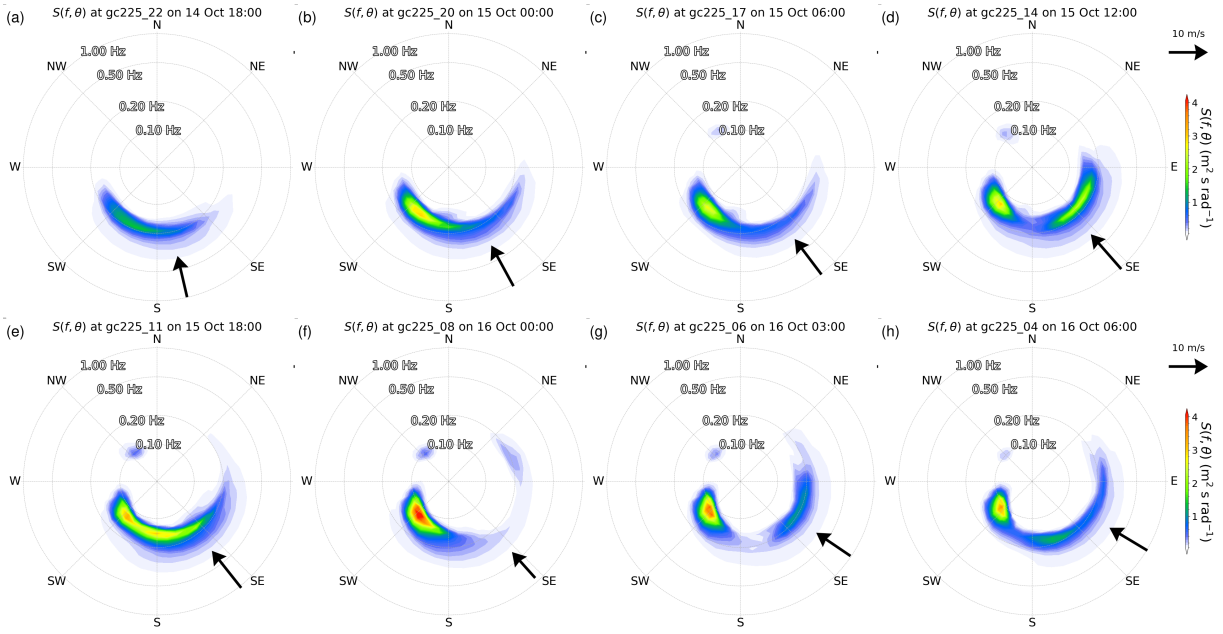

FIG. 6: Swell tracking of the crossing swell energy from the generation on 14 Oct to the MIZ arrival on 16 Oct. TodaiWW3-ArCS frequency-directional spectra $S(f,\theta)$ are shown at (a) gc225_22 on 18:00 14 Oct, (b) gc225_20 on 00:00 15 Oct, (c) gc225_17 on 06:00 15 Oct, (d) gc225_14 on 12:00 15 Oct, (e) gc225_11 on 18:00 15 Oct, (f) gc225_08 on 00:00 16 Oct, (g) gc225_06 on 03:00 16 Oct, and (h) gc225_04 on 06:00 16 Oct. The higher gc225_# numbers are located farther from the MIZ (i.e.,near the Siberian coast). The black arrows indicate the wind vector at each output point.

were the lowest at this time compared to the other directional spectra shown in Figure 6. By g and h, the spectra were bimodal with the distinct wind-sea and swell peaks; the crossing swell slowly decayed and narrowed as the waves approached and entered the MIZ.

5. The role of the nonlinear interactions source term

a. Weak interactions between wind input and crossing swell

The propagation of the southwesterly energy as crossing swell under the southeasterly winds in the hindcast model seems robust. Since these waves were oblique to the wind directions, they could not grow under the direct influence of wind input, but they grew due to nonlinear interactions. The source terms were examined to elucidate the role of s_{nl} in the swell evolution over a long distance.

The directional features of s_{nl} corresponding to Figure 6 can be grouped in either nonlinear growth of the crossing swell due to wind or weak interactions between wind input and swell. The shape of s_{nl} is markedly different for the two cases, and the presence of a wind-sea peak may be

Accepted for publication in *Journal of Physical Oceanography*. DOI 10.1175/JPO-D-24-0251.1.

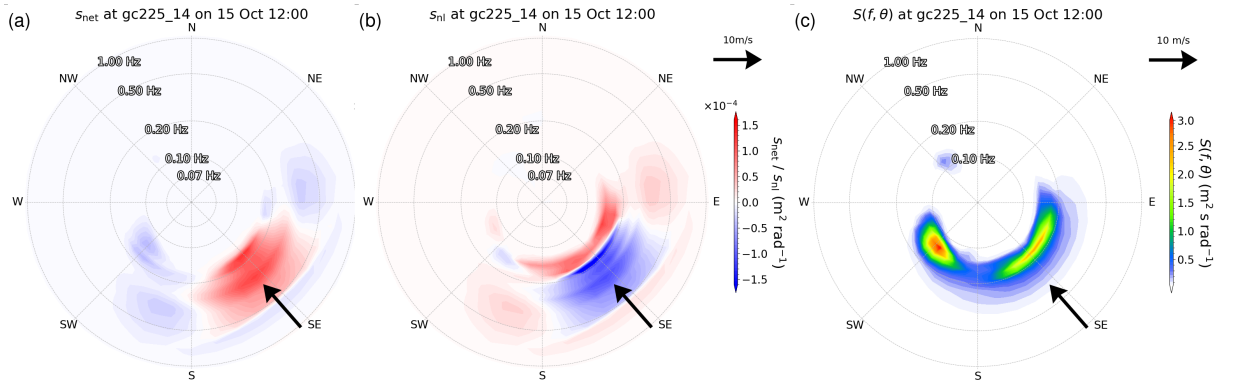

FIG. 7: TodaiWW3-ArCS source terms (a) s_{net}, and (b) s_{nl}, and (c) the frequency-directional spectrum $S(f,\theta)$ are shown at gc225_14 on 12:00 15 Oct. The black arrows indicate the wind vector. Note that $S(f,\theta)$ is the same as Fig 6d.

a key factor: s_{nl} for Figures 6d and g shows weak interactions between the wind and the crossing swell spectral peak when there is a distinct wind-sea peak. We first discuss this case because its shape is analogous to the s_{nl} shape as described in Young and Van Vledder (1993).

Source terms were split into the net source term energy s_{net} (s_{in}+s_{ds}+s_{bot}) and s_{nl} because s_{net} represents the energy that was generated and dissipated while s_{nl} acts to redistribute energy among spectral components. The source terms and the directional spectrum at gc225_14 (corresponding to Figure 6d) are shown in Figure 7. s_{net} here is primarily a balance between s_{in} and s_{ds}, and most of the action resides in the frequency space $\frac{f}{f_{\mathrm{w}}} > 1$ where f_{w} is the peak of wind-sea energy. The difference between the s_{in} and s_{ds} directional spreading determines the shape of s_{net}; s_{in} acts approximately within ±30 degrees to the wind direction whereas s_{ds} acts over a much broader region (e.g., >90 degrees). The magnitude of s_{in} was larger than that of s_{ds}, and as such, s_{net} around the wind vector has positive net energy. There is frequency space that has net energy loss at $f > 0.5$ Hz over the directional sector of net energy in, meaning s_{ds} acts at higher frequencies than s_{in}. s_{in} and s_{ds} are bimodal along the frequency space with a peak at the wind-sea spectral peak and another at a higher frequency of $f \approx 0.35$ Hz. At the crossing swell spectral peak f_{s}, the energy decays due to s_{ds} (and therefore s_{net}).

The role of s_{nl} in the $\frac{f}{f_{\mathrm{w}}} > 1$ frequency space is clear and practically a reciprocal of s_{net}. The energy input from s_{in} is almost completely redistributed to other regions of the spectrum. Some energy was moved to fill the net energy loss in the $\frac{f}{f_{\mathrm{w}}} > 1$ space, such as the lobes on either sides of s_{in}, and as a result, this frequency space primarily consists of $s_{\mathrm{tot}} \approx 0$ (not shown here). s_{nl}

Accepted for publication in *Journal of Physical Oceanography*. DOI 10.1175/JPO-D-24-0251.1.

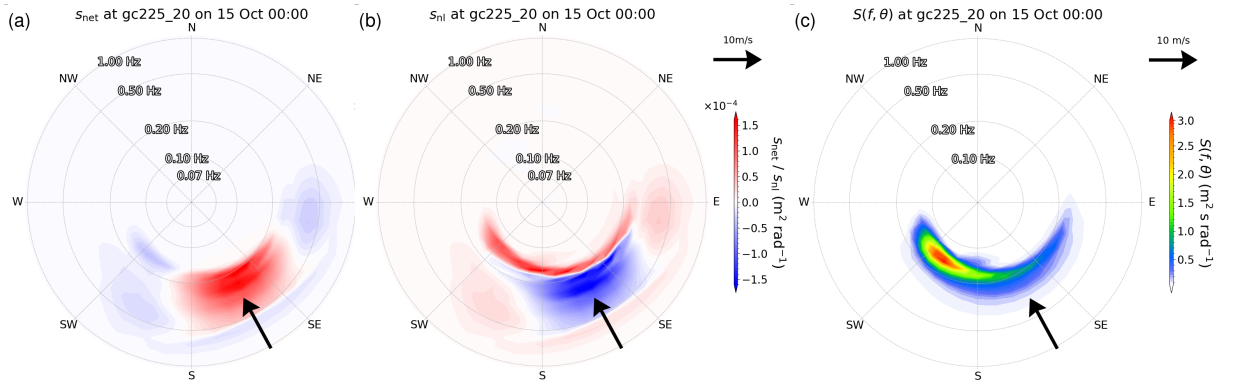

FIG. 8: TodaiWW3-ArCS source terms (a) s_{net}, and (b) s_{nl}, and (c) the frequency-directional spectrum $S(f,\theta)$ are shown at gc225_20 on 00:00 15 Oct. The black arrows indicate the wind vector. Note that $S(f,\theta)$ is the same as Figure 6b.

on its own appears to be forcing the spectrum to be directionally broader, but its total effect is balanced among the source terms; as described in Young et al. (1987), this implies that this part of the spectrum is in quasi-equilibrium and is responsible for the fetch or duration independent shape of the high-frequency tail of the spectrum.

In the frequency space $\frac{f}{f_{\mathrm{w}}} \leq 1$, the net energy input from the wind is being transferred to the lower frequencies with a directional spread of ±45 degrees to the wind direction. The redistributed energy acts to downshift the wind-sea spectral peak frequency, while its frequency width is narrowest along the wind direction and broader at the oblique angles.

b. Nonlinear growth of the crossing swell

The second group of the s_{nl} shapes corresponding to Figure 6 frequency-directional spectra is nonlinear growth of the crossing swell due to wind; this is the process by which the crossing swell evolved and propagated to the MIZ buoys and occurs when there is nonlinear coupling between the wind input energy and the crossing swell spectral peak. Two cases of directional spectra for nonlinear growth are shown. The first case is at gc225_20 where the crossing swell began to grow as shown in Figure 8.

s_{net} is similar to that of Figure 7 because the shape of s_{in} and s_{ds} were also similar. s_{in} was directionally narrower than s_{ds}, resulting in similar net energy distributions. The subtle difference is that the bimodality in the frequency space was less clear, perhaps because the wind-sea peak was ambiguous. Although the primary role of s_{nl} is still the same (i.e., redistributing net energy to the

Accepted for publication in *Journal of Physical Oceanography*. DOI 10.1175/JPO-D-24-0251.1.

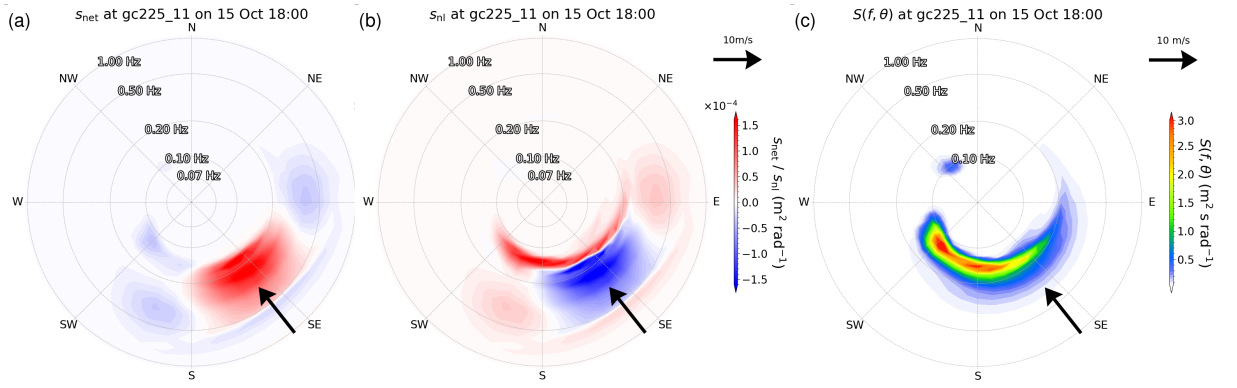

FIG. 9: TodaiWW3-ArCS source terms (a) s_{net}, and (b) s_{nl}, and (c) the frequency-directional spectrum $S(f,\theta)$ are shown at gc225_11 on 18:00 15 Oct. The black arrows indicate the wind vector. Note that $S(f,\theta)$ is the same as Figure 6e.

lower frequency space of the spectrum), the shape of s_{nl} in the frequency space $\frac{f}{f_p} \leq 1$ is markedly different to that of Figure 7. s_{nl} redistributes energy over a broad angle of more than 135 degrees near $f \approx f_p$ and the energy distribution is skewed towards the crossing swell direction. In fact, more energy was moved to the crossing swell spectral peak rather than along the wind direction. Since the redistributed energy was greater than that of the net energy loss, the crossing swell grew as a result of the nonlinear coupling of the wind input energy and the old spectral peak. While s_{nl} still redistributes energy to the wind-sea sector of the spectrum, the nonlinear growth of the old spectral peak inhibits the wind-sea growth.

Another case is shown at gc225_11 in Figure 9, which has similar characteristics in general to Figure 8, but the directional spectrum now has two peaks that are not aligned to the wind direction. One was the southwesterly crossing swell, and the other was southerly energy. The traits of s_{net} and s_{nl} remained similar, but s_{nl} was not as directionally spread as in the previous case, and more energy was redistributed to the direction in between the swell peak and wind direction. Within the next couple of model output time steps of 6 hours, the spectrum became unimodal with a peak more aligned to the wind direction, perhaps because the transient wave systems (the southerly and southwesterly waves) passed this location.

6. Idealized cross-sea simulations using the DIA and EXACT-NL models

We have presented hindcast evidence that waves measured by the drifting wave buoys in the MIZ were crossing swell that traveled hundreds of kilometers and evolved due to nonlinear interactions.

Accepted for publication in *Journal of Physical Oceanography*. DOI 10.1175/JPO-D-24-0251.1.

To consolidate the findings, we conducted numerical simulations of idealized cross-sea cases to ensure the hindcast evidence is reproduced using the same DIA parameterization, but also using the full Boltzmann model of Hasselmann's integral (Eq. 2). The EXACT-NL model, as an implementation of the full Boltzmann integral in WAVEWATCH III (the NL2 switch (WW3DG 2019)), requires 10^3 to 10^4 times more computational resources than the DIA method. While synoptic scale simulations using the EXACT-NL model have been performed experimentally (Ponce de León et al. 2018; Liu et al. 2021), its use for synoptic scale simulations is still considered too cumbersome and most operational models adopt the DIA method for the nonlinear interactions source term. Therefore, EXACT-NL was used in the idealized cross-sea simulations to verify that the effect of the s_{nl} as seen in the hindcast using the DIA method is valid compared to the full Boltzmann computation. The idealized simulation setup adopted one of the WAVEWATCH III Regression Tests named "*ww3_ts2*".

The model domain has 24 grids in the zonal orientation with a spatial resolution of 25 km (the model domain extends 600 km). Lateral boundary conditions were imposed at the westernmost grid (i.e., X= 0), so there were 23 active grids and 1 boundary grid. Westerly swell was imposed at the boundary grid to resemble the results of the crossing swell propagation. Winds at various oblique directions were forced, and the shape of s_{nl} was analyzed. The swell boundary conditions were produced in a separate run, in which the model domain was extended westward to X= −300 km and the simulation start time was −3 days. Steady 8 ms^{-1} westerly wind was forced and the wave spectra at the boundary grid X= 0 formed the swell lateral boundary conditions. A series of idealized cross-sea simulations (i.e., swell+wind cases) were conducted for various wind directions, and wave spectra and source terms were obtained at each active grid.

The wave growth for identical conditions between the DIA and EXACT-NL differed in the idealized simulations. The peak and mean periods for the EXACT-NL model were higher than that of the DIA periods; as such, the propagation of the waves across the model domain was changed. This meant that spectral evolution was compared at different time steps and locations. Figure 10 is a comparison of s_{nl} at the similar stages of directional spectrum developments (i.e., the wind-sea and swell frequencies are close to each other) for DIA and EXACT-NL results. Under the idealized cross-sea condition at 80 degree angle between constant wind and the swell propagating into the computational domain from the western boundary, both s_{nl} computations were consistent with the

Accepted for publication in *Journal of Physical Oceanography*. DOI 10.1175/JPO-D-24-0251.1.

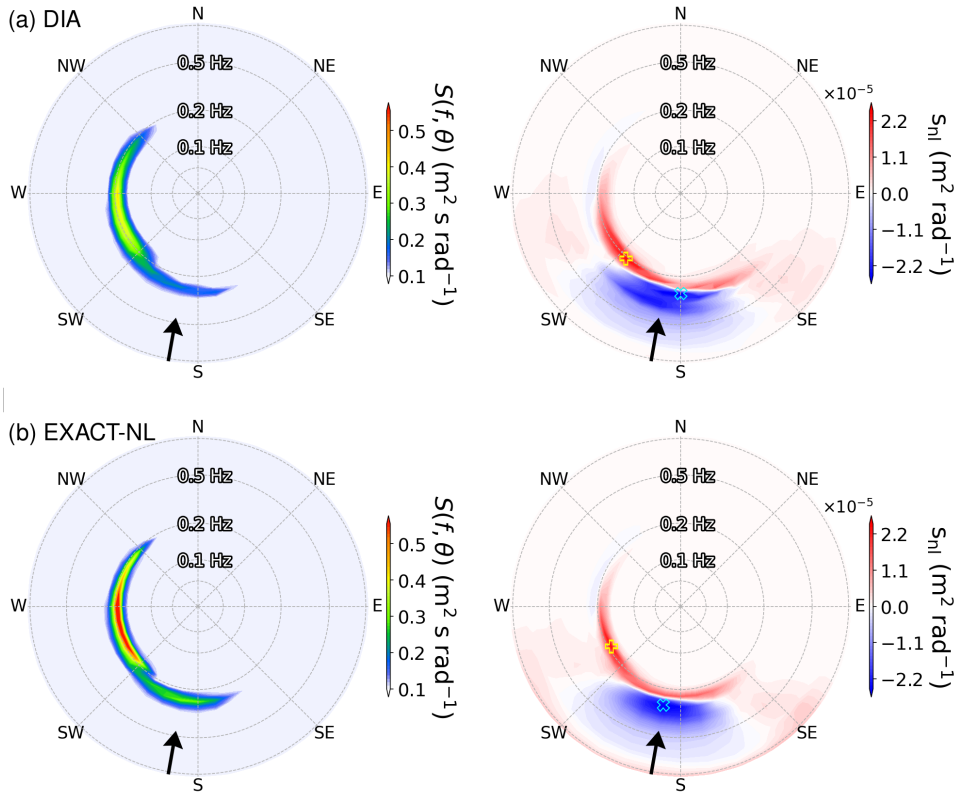

FIG. 10: Idealized cross-sea simulations in which westerly swell was imposed at the boundary and oblique wind at 190 degrees was forced with wind speed of 8 m/s. Simulations for the DIA method (t=4 hr, x=100 km) (a) and the EXACT-NL model (t=8 hr, x=100 km) (b) were conducted to compare the effects of the different nonlinear interactions source terms. The left panels show the directional spectrum and the right side is s_{nl}. Yellow "plus" and cyan "X" markers indicate the s_{nl} maxima and minima, respectively. The black arrow is a wind vector from 190 degrees.

hindcast results, reproducing the wind-sea growth rate inhibition along the wind direction and transfer of energy towards the oblique swell direction. An apparent difference between the DIA method compared to the EXACT-NL model is that peaks and troughs appear to split whereas the EXACT-NL shows smoother energy distribution. It is also noted that, although the redistribution of wind input energy reaches the westerly swell components, the peak steering of the wind sea appears to be 40 and 50 degrees oblique to the wind direction as shown by the "plus" and "X" markers indicating the s_{nl} maxima and minima, respectively (see the right panels of Figure 10). The steering is more oblique than Masson (1993) estimated, and it also implies the swell direction is slowly changing due to oblique wind. Another interpretation is that a new wave system develops between the swell and wind direction. Under the steady wind conditions, the wind-sea peak will eventually evolve and becomes the dominant energy.

Accepted for publication in *Journal of Physical Oceanography*. DOI 10.1175/JPO-D-24-0251.1.

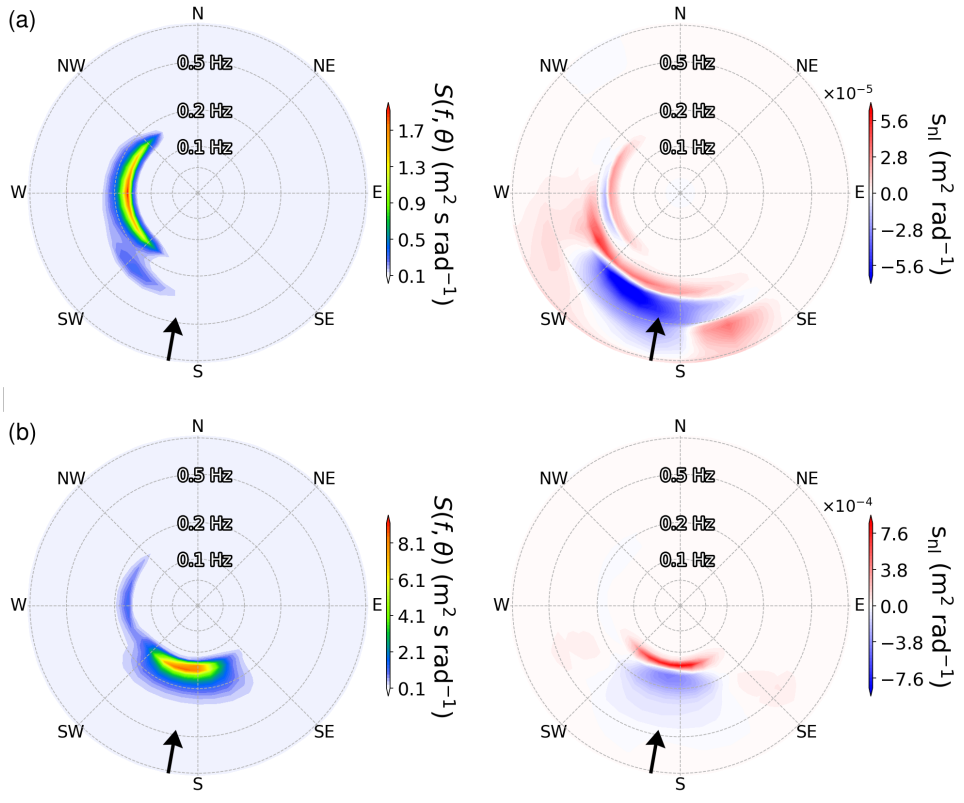

FIG. 11: Idealized cross-sea simulations based on the EXACT-NL model. a) the wind sea and swell do not interact directly because of the frequency separation is too large ($f_w = 0.27$ Hz and $f_s = 0.15$ Hz, so $\frac{f_s}{f_w} = 0.56$), although the wind-sea direction is still steered towards the swell direction. The time was t=2 hr and x=50 km. b) when the E_w becomes dominant, the nonlinear transfer of energy to the swell becomes weak. For this condition the time was t=8 hr and x=50 km. The black arrow is a wind vector, which was 8 ms^{-1} from 190 degrees.

The previous paragraph confirmed the nonlinear coupling between the swell and wind sea for oblique angles using both the DIA and EXACT-NL models under certain conditions. Using the EXACT-NL results, we further present insights into how the balance between wind-sea and swell energy (E_s and E_w) affects their interactions. At the outset of the wind-sea growth, $E_w << E_s$ & $f_w > f_s$, the shape of s_{nl} is distinctly different from that of s_{nl} we have discussed thus far. The nonlinear interactions are not directly coupled as shown in Figure 11a; more specifically, the wind sea is interacting with the higher frequency spectral components than the peak of the swell system, and the swell has its own nonlinear interactions response. Once the f_w and f_s are close to each other (e.g., $\frac{f_s}{f_w} > 0.6$ as will be described below), but $E_w < E_s$, swell grows via the nonlinear coupling of the waves as discussed in the previous paragraph and Section 5b. As the wind sea develops and

Accepted for publication in *Journal of Physical Oceanography*. DOI 10.1175/JPO-D-24-0251.1.

$E_w > E_s$, the interactions appear to become weak (see Figure 11b), which is consistent with the case from the hindcast as discussed in Section 5a.

The nonlinear interactions behavior observed in the idealized simulations bears analogy with the Masson (1993) theory. The Masson (1993) expression of the Hasselmann integral (Eq. 2) using the energy density instead of the action density is as follows:

$$\frac{\partial S(\omega_4,\theta_4)}{\partial t} = \omega_p^{11}\hat{\omega}_4 \iiint G'\delta(\hat{\mathbf{k}}_1+\hat{\mathbf{k}}_2-\hat{\mathbf{k}}_3-\hat{\mathbf{k}}_4)\delta(\hat{\omega}_1+\hat{\omega}_2-\hat{\omega}_3-\hat{\omega}_4) \tag{4}$$

$$\times\left[S_1S_2(\hat{\omega}_4^4S_3+\hat{\omega}_3^4S_4)-S_3S_4(\hat{\omega}_2^4S_1+\hat{\omega}_1^4S_2)\right]d\hat{\omega}_{1,2,3}d\theta_{1,2,3}.$$

The " $\hat{}$ " denotes the normalized frequency and wavenumber, e.g., $\hat{\omega} = \omega/\omega_p$ where ω_p is the frequency of the spectral peak. Following Hasselmann (1963) and Masson (1993), the time derivative of swell variance E_s can be obtained using $S_s = E_s\delta(\omega-\omega_s,\theta-\theta_s)$, i.e., assuming a narrow swell system distinctly separated from the wind-sea spectrum. Replacing S_4 and ω_4 in Eq. 4 with the narrow swell and after integration in the neighborhood of the swell, the rate of change of E_s,

$$\frac{dE_s}{dt} = \iiint \omega_p^{11}\hat{\omega}_sG'\delta(\hat{\mathbf{k}}_1+\hat{\mathbf{k}}_2-\hat{\mathbf{k}}_3-\hat{\mathbf{k}}_s)\delta(\hat{\omega}_1+\hat{\omega}_2-\hat{\omega}_3-\hat{\omega}_s)\times\left[S_1S_2S_3\hat{\omega}_s^4\right]d\hat{\omega}_{1,2,3}d\theta_{1,2,3} \tag{5}$$

$$-E_s\iiint \omega_p^{11}\hat{\omega}_sG'\delta(\hat{\mathbf{k}}_1+\hat{\mathbf{k}}_2-\hat{\mathbf{k}}_3-\hat{\mathbf{k}}_s)\delta(\hat{\omega}_1+\hat{\omega}_2-\hat{\omega}_3-\hat{\omega}_s)\times\left[-S_1S_2\hat{\omega}_3^4+S_3S_1\hat{\omega}_2^4+S_2S_3\hat{\omega}_1^4\right]d\hat{\omega}_{1,2,3}d\theta_{1,2,3},$$

is derived. For $E_s > E_w$ and assuming the wind-sea spectrum to be stationary, we can neglect the first term in Eq. 5 and arrive at the same exponential decay rate of E_s as Eq. 7 in Masson (1993). As described in Introduction, Masson (1993) found that for bimodal wind-sea and swell sea states, there is a region in the frequency-direction space where the decay rate is negative when the swell frequency approaches the wind-sea spectral peak $\frac{\omega_s}{\omega_w} > 0.6$; indeed, Masson (1993) showed that swell grows at the expense of short waves due to nonlinear interactions transferring wind-sea energy to the swell. Beyond the highly idealized representation of the swell as a delta function, we may consider a narrow banded swell energy defined as $E_s = \langle S_4\rangle_{\Omega_s} = \iint_{\Omega_s} S_4\, d\omega_4\, d\theta_4$ or $\langle S_4\rangle_{\Omega_s} = \iint_{\Omega_s} S_4\,\mathbf{J}(\boldsymbol{\kappa}')\, d\boldsymbol{\kappa}'$ in the neighborhood of (ω_s,θ_s) where $\mathbf{J}$ is the Jacobian. The swell is assumed to be contained within $\hat{\mathbf{k}}_s+\boldsymbol{\kappa}'$ and $(\hat{\omega}_s+\omega')^2 = g|\hat{\mathbf{k}}_s+\boldsymbol{\kappa}'|$, and $\hat{\mathbf{k}}_s >> \boldsymbol{\kappa}'$. An extension of Masson's theory may be expressed as

Accepted for publication in *Journal of Physical Oceanography*. DOI 10.1175/JPO-D-24-0251.1.

$$\frac{dE_s}{dt} = -\left\langle S_4(\hat{\mathbf{k}}_s + \boldsymbol{\kappa}') \iiint_{\Omega-\Omega_s} \omega_p^{11}(\hat{\omega}_s + \omega') G' \delta(\hat{\mathbf{k}}_1 + \hat{\mathbf{k}}_2 - \hat{\mathbf{k}}_3 - (\hat{\mathbf{k}}_s + \boldsymbol{\kappa}')) \right.$$
$$\left. \delta(\hat{\omega}_1 + \hat{\omega}_2 - \hat{\omega}_3 - (\hat{\omega}_s + \omega')) \times \left[-S_1 S_2 \hat{\omega}_3^4 + S_3 S_1 \hat{\omega}_2^4 + S_2 S_3 \hat{\omega}_1^4 \right] d\hat{\omega}_{1,2,3}\, d\theta_{1,2,3} \right\rangle . \quad (6)$$

From Eq. 6, it is not apparent whether the swell energy grows exponentially. The numerical experiment discussed in this section showed that the swell energy grew, extracting energy from the wind sea, and suggests that Eq. 5 is a good approximation to Eq. 6.

A careful consideration of Eqs. 5 and 6 and the assumptions therein suggest Masson (1993)'s theory appears to be valid only at the very initial stage of the swell and wind-sea interaction because when the swell starts to grow by extracting the wind-sea energy, the assumption of the wind-sea spectrum being stationary fails. However, our idealized simulations included the presence of wind, so the wind input may compensate for the loss of wind-sea energy and allow the swell to continue growing. Moreover, the large difference in the wind and swell propagation directions assures that the direct wind energy input to swell is negligible. Another observation of the simulation results is that the wind input cannot be arbitrary because the balance between s_{in} and s_{nl} appears to be important: as the wind sea grows, the transfer to the swell slows down and becomes negligible when the wind-sea spectrum becomes dominant. This point is important to translate the interpretation of the idealized case results to the hindcast finding. It is our conjecture that the southwesterly swell grew by extracting wind input energy, which still played an important role for swell growth when the difference angle between the swell and the wind was more oblique than the optimum angle for maximum energy exchange. What may be remarkable is that the southwesterly swell survived through the southeasterly wind-sea field under the right balance of wind-sea and swell energy and spectral peaks ($\frac{\omega_s}{\omega_w} > 0.6$) over hundreds of kilometers (i.e., spatial evolution of the wind sea was in balance with the transient swell such that it grew). It should be emphasized that we are not claiming high accuracy of wind forcing and model physics as we are unable to validate the swell growth all along its propagation path; but rather, the hindcast using the DIA method and the idealized cross-sea simulations using both the DIA and EXACT-NL models provide robust evidence that the nonlinear coupling of the wind sea and the swell was central to the evolution of the southwesterly swell measured by the Spotters in the MIZ.

Accepted for publication in *Journal of Physical Oceanography*. DOI 10.1175/JPO-D-24-0251.1.

7. Conclusions

A spectral wave model, named TodaiWW3-ArCS using the Discrete Interaction Approximation (DIA) method as its nonlinear interactions source term s_{nl}, simulated swell evolution under the cross-sea condition over hundreds of kilometers in the ice-free Arctic Ocean. Central to the swell development was the nonlinear coupling of wind energy input and swell energy via s_{nl}. In our hindcast model, the southwesterly swell energy first developed near the Siberian coast. The wind turned southeast, but the swell energy continued to propagate towards the marginal ice zone (MIZ) located north of the Chukchi Sea. The southwesterly swell continued to grow because the wind input energy was redistributed to the swell part of the spectrum, i.e., the wind input energy was taken away to the swell energy. The nonlinear coupling between wind input and swell was found to occur for difference angles up to 90 degrees.

The swell evolution under a cross sea was investigated because four drifting wave buoys located in the MIZ measured southwesterly waves while the local wind was southeasterly. Swell tracking of the southwesterly waves led us to find that the southwesterly swell originated from the Siberian coast where the south-southwest wind generated a broad wind-sea peak that included energy in the southwest direction. Following the onset of the southwesterly energy, the wind was consistently southeast but the southwesterly swell continued to propagate in the ice-free ocean and eventually into the MIZ. The buoy-measured wave heights, periods, and directions agreed qualitatively with the hindcast model results, justifying the use of TodaiWW3-ArCS for our study. The cross sea is a well-known shipping hazard (Toffoli et al. 2005), and as such, it presents a potential shipping hazard in the Arctic Ocean. The southwesterly swell signal in the buoy data was conspicuous, perhaps because the wind-sea energy was mostly suppressed by the presence of the sea ice. This demonstrates wave observations and results therein in the ice-covered seas can cross over to findings in the general ocean wave physics.

Our results suggest that the swell can grow by extracting wind input energy from oblique wind directions via the nonlinear interactions source term. Because the DIA method used for s_{nl} in the hindcast model is an approximation that only considers limited quadruplet interactions, the hindcast finding needed to be corroborated against a more complete s_{nl} computation. Accordingly, idealized cross-sea simulations were conducted using the EXACT-NL model, a full Boltzmann model of Hasselmann's integral, and its results were compared to the results using the DIA. The idealized

Accepted for publication in *Journal of Physical Oceanography*. DOI 10.1175/JPO-D-24-0251.1.

cross-sea simulation comprised of westerly swell was imposed at the westernmost grid point in the model domain that extended 600 km along the zonal orientation. Results were discussed for the case when the wind was forced with the difference angle of 80 degrees.

The EXACT-NL simulations were consistent with the hindcast results using the DIA method: both models reproduced the inhibition of wind-sea growth rate and energy redistribution from the wind input region to the swell space. The full Boltzmann computation results were analyzed further to investigate mechanisms of the wind energy transfer to the swell. We observed the peak steering of the wind energy towards the swell can be as oblique as 50 degrees and the balance between the wind-sea and swell spectral peaks, e.g., $\frac{f_s}{f_w} > 0.6$, was key for nonlinear swell growth by wind under a cross-sea condition. The nonlinear interactions behavior was found to be consistent with Masson (1993) who showed that a narrow swell system grows exponentially due to nonlinear coupling of swell and wind sea for a given condition when the swell spectral peak frequency approaches that of the wind sea. Based on the derivation of the exponential swell decay/growth rate, the Masson (1993) theory appears to be valid only at the very initial stage of the swell and wind-sea interaction because the assumption of a stationary wind-sea spectrum fails as soon as the swell starts to grow exponentially. In the idealized simulations under the presence of wind, swell growth may persist longer because the wind input can compensate for the loss of wind-sea energy due to nonlinear transfer; however, the wind input cannot be arbitrary because the balance between s_{in} and s_{nl} appears to be important and when the $E_s > E_w$ condition breaks down, the wind sea no longer interacts with the swell. The Masson (1993) expression of the swell decay rate for swell with a finite spectral bandwidth was also derived. The numerical experiment results suggest the exponential decay rate assuming swell to be a delta function is a good approximation to the narrow banded swell system. Moreover, the idea that wind input can compensate for the wind-sea spectrum no longer being stationary may be a hypothesis that extends the Masson (1993) theory under the presence of wind. These ideas, however, warrant further investigations. A striking feature of the hindcast results was that the model simulated the swell propagation in the right balance with the southeasterly wind-sea field, such that the swell grew over hundreds of kilometers in the ice-free ocean. The modeled swell then propagated into the MIZ, and, remarkably, agreed well with the buoy-measured waves.

Accepted for publication in *Journal of Physical Oceanography*. DOI 10.1175/JPO-D-24-0251.1.

Acknowledgments. We are grateful to the R/V Mirai crew on board MR20-05C for deploying the drifting wave buoys. This work was a part of the Arctic Challenge for Sustainability II (ArCS II) Project (Program Grant Number JPMXD1420318865). This work was also supported by JSPS under KAKENHI Grant Number 19H00801, 19H05512, 21K14357, and 22H00241. AA acknowledges support from EPSRC (EP/Y02012X/1) and DAIWA Anglo-Japanese Foundation (14512/15357).

Data availability statement. The wave buoy data, and model grid and spectra/source term outputs are registered at the Arctic Data archive System (https://ads.nipr.ac.jp/) maintained by the National Institute of Polar Research, Japan. The data DOIs are https://ads.nipr.ac.jp/dataset/A20241112-006, https://ads.nipr.ac.jp/dataset/A20241101-011, and https://ads.nipr.ac.jp/dataset/A20241101-010, respectively.

Accepted for publication in *Journal of Physical Oceanography*. DOI 10.1175/JPO-D-24-0251.1.

APPENDIX A

TodaiWW3-ArCS and Spotter data comparison

The wave model outputs used in this study were compared with the Spotter buoy measurements in the main text in Section 3*a*. In Figure 3, wave height H_s, mean period, T_{0m1} and mean direction D_m comparisons were shown. To complement Figure 3, the comparisons for the peak period T_p and the peak direction D_p are shown in Figure A1, which also shows similar trends as described in the main text.

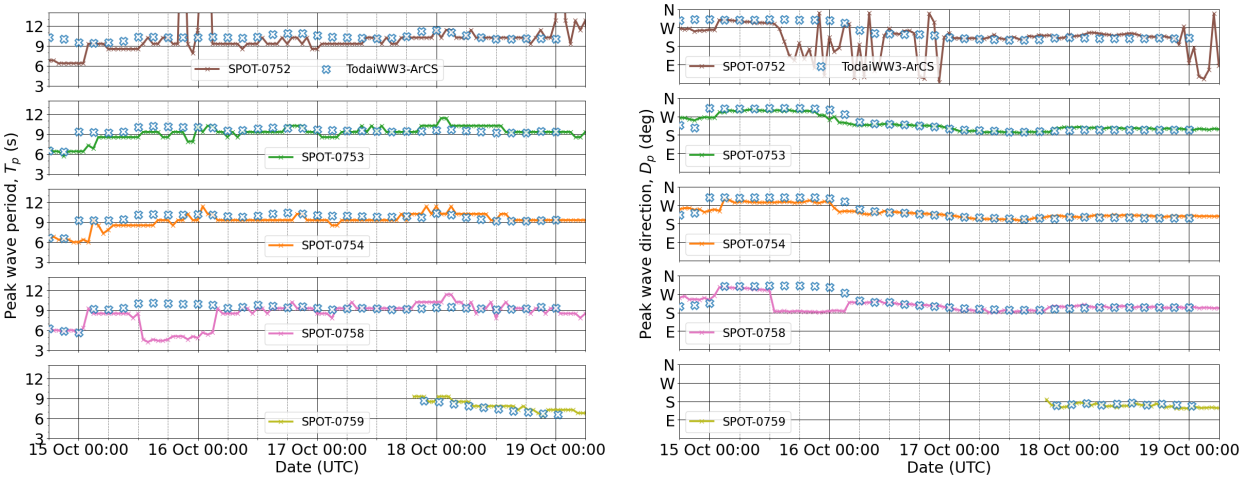

(a) Peak wave period T_p.

(b) Mean wave direction D_p.

FIG. A1: Comparison of TodaiWW3-ArCS and Spotter buoy wave statistics during the wave event: (a) peak period T_p and (b) peak wave direction D_p.

Accepted for publication in *Journal of Physical Oceanography*. DOI 10.1175/JPO-D-24-0251.1.

APPENDIX B

The onset of southweterly swell energy

We discussed in Section 4*a* that the initial southwesterly swell energy was generated near the Siberian coast along the southwesterly propagation path at gc225_24 on 12:00 14 Oct 2020. The nonlinear interactions source term is shown in the main text in Figure 4a, and the frequency-directional spectrum is shown here in Figure B1 to demonstrate that the energy resides in the southwest directional space.

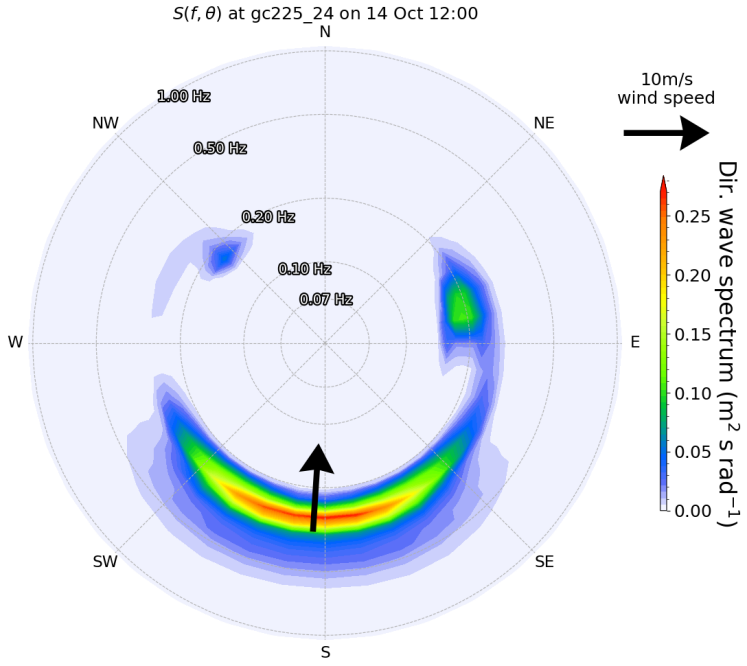

FIG. B1: Frequency-directional spectrum at gc225_24 on 12:00 14 Oct 2020 when the onset of southwesterly wave energy was identified.

Accepted for publication in *Journal of Physical Oceanography*. DOI 10.1175/JPO-D-24-0251.1.

References

Alberello, A., E. I. Părău, Q. Liu, and F. De Santi, 2024: Evolution of wave directional properties in sea ice. *Ocean Modelling*, **188**, 102 305, https://doi.org/https://doi.org/10.1016/j.ocemod.2023.102305.

Ardhuin, F., T. H. C. Herbers, K. P. Watts, G. P. van Vledder, R. Jensen, and H. C. Graber, 2007: Swell and slanting-fetch effects on wind wave growth. *Journal of Physical Oceanography*, **37 (4)**, 908 – 931.

Donelan, M. A., J. Hamilton, W. H. Hui, and R. W. Stewart, 1985: Directional spectra of wind-generated ocean waves. *Philosophical Transactions of the Royal Society of London. Series A, Mathematical and Physical Sciences*, **315 (1534)**, 509–562.

Hasselmann, K., 1962: On the non-linear energy transfer in a gravity-wave spectrum part 1. general theory. *Journal of Fluid Mechanics*, **12 (4)**, 481–500, https://doi.org/10.1017/S0022112062000373.

Hasselmann, K., 1963: On the non-linear energy transfer in a gravity-wave spectrum. part 3. evaluation of the energy flux and swell-sea interaction for a neumann spectrum. *Journal of Fluid Mechanics*, **15 (3)**, 385–398, https://doi.org/10.1017/S002211206300032X.

Hasselmann, K., and Coauthors, 1973: Measurements of wind-wave growth and swell decay during the Joint North Sea Wave Project (JONSWAP). Tech. Rep. A8 (Suppl.), no. 12, Dt. hydrogr. Z., 1-95 pp.

Hasselmann, S., and K. Hasselmann, 1985: Computations and parameterizations of the nonlinear energy transfer in a gravity-wave spectrum. Part I: A new method for efficient computations of the exact nonlinear transfer integral. *Journal of Physical Oceanography*, **15 (11)**, 1369 – 1377, https://doi.org/10.1175/1520-0485(1985)015⟨1369:CAPOTN⟩2.0.CO;2.

Hasselmann, S., K. Hasselmann, J. H. Allender, and T. P. Barnett, 1985: Computations and parameterizations of the nonlinear energy transfer in a gravity-wave specturm. Part II: Parameterizations of the nonlinear energy transfer for application in wave models. *Journal of Physical Oceanography*, **15 (11)**, 1378 – 1391, https://doi.org/10.1175/1520-0485(1985)015⟨1378:CAPOTN⟩2.0.CO;2.

Accepted for publication in *Journal of Physical Oceanography*. DOI 10.1175/JPO-D-24-0251.1.

Herman, A., 2024: From apparent attenuation towards physics-based source terms – a perspective on spectral wave modeling in ice-covered seas. *Front. Marine Science*, **11**, https://doi.org/10.3389/fmars.2024.1413116.

Herman, A., and K. Bradtke, 2024: Fetch-limited, strongly forced wind waves in waters with frazil and grease ice – spectral modeling and satellite observations in an Antarctic coastal polynya. *Journal of Geophysical Research: Oceans*, **129 (4)**, e2023JC020 452, https://doi.org/10.1029/2023JC020452.

Hersbach, H., and Coauthors, 2023: ERA5 hourly data on single levels from 1940 to present. Copernicus Climate Change Service (C3S) Climate Data Store (CDS), accessed on 15-OCT-2024, https://doi.org/10.24381/cds.adbb2d47.

Jakobsson, M., and Coauthors, 2012: The International Bathymetric Chart of the Arctic Ocean (IBCAO) Version 3.0. *Geophysical Research Letters*, **39 (12)**, L12 609, https://doi.org/10.1029/2012GL052219.

Jones, I. S. F., and Y. Toba, Eds., 2001: *Wind Stress over the Ocean*. Cambridge University Press.

Liu, Q., O. Gramstad, and A. Babanin, 2021: Kinetic equations in a third-generation spectral wave model. *Journal of Fluid Mechanics*, **910**, A50, https://doi.org/10.1017/jfm.2020.1036.

Liu, Q., W. E. Rogers, A. V. Babanin, I. R. Young, L. Romero, S. Zieger, F. Qiao, and C. Guan, 2019: Observation-based source terms in the third-generation wave model WAVEWATCH III: Updates and verification. *Journal of Physical Oceanography*, **49 (2)**, 489–517, https://doi.org/https://doi.org/10.1175/JPO-D-18-0137.1.

Masson, D., 1993: On the nonlinear coupling between swell and wind waves. *Journal of Physical Oceanography*, **23 (6)**, 1249 – 1258, https://doi.org/10.1175/1520-0485(1993)023⟨1249:OTNCBS⟩2.0.CO;2.

Nose, T., T. Waseda, T. Kodaira, and J. Inoue, 2020: Satellite-retrieved sea ice concentration uncertainty and its effect on modelling wave evolution in marginal ice zones. *The Cryosphere*, **14 (6)**, 2029–2052, https://doi.org/10.5194/tc-14-2029-2020.

Accepted for publication in *Journal of Physical Oceanography*. DOI 10.1175/JPO-D-24-0251.1.

Nose, T., A. Webb, T. Waseda, J. Inoue, and K. Sato, 2018: Predictability of storm wave heights in the ice-free Beaufort Sea. *Ocean Dynamics*, **68 (10)**, 1383–1402, https://doi.org/10.1007/s10236-018-1194-0.

Pettersson, H., K. K. Kahma, and L. Tuomi, 2010: Wave directions in a narrow bay. *Journal of Physical Oceanography*, **40 (1)**, 155 – 169.

Ponce de León, S., A. Osborne, and C. Guedes Soares, 2018: On the importance of the exact nonlinear interactions in the spectral characterization of rogue waves. *International Conference on Offshore Mechanics and Arctic Engineering*, **Volume 3: Structures, Safety, and Reliability**, V003T02A001, https://doi.org/10.1115/OMAE2018-77270.

Rogers, W. E., A. V. Babanin, and D. W. Wang, 2012: Observation-consistent input and white-capping dissipation in a model for wind-generated surface waves: Description and simple calculations. *Journal of Atmospheric and Oceanic Technology*, **29 (9)**, 1329–1346, https://doi.org/10.1175/JTECH-D-11-00092.1.

Rogers, W. E., and T. J. Campbell, 2009: Implementation of curvilinear coordinate system in the WAVEWATCH III model. Tech. Rep. NRL/MR/7320–09-9193, Naval Research Laboratory, Stennis Space Center.

Smith, G. C., and Coauthors, 2021: The Regional Ice Ocean Prediction System v2: a pan-canadian ocean analysis system using an online tidal harmonic analysis. *Geoscientific Model Development*, **14 (3)**, 1445–1467, https://doi.org/10.5194/gmd-14-1445-2021.

Tamura, H., K. Kawaguchi, T. Iwamoto, and T. Fujiki, 2021: Coastal destruction and unusual wave spectra induced by typhoon faxai in 2019. *Coastal Engineering Journal*, **63 (1)**, 92–105.

Tamura, H., T. Waseda, and Y. Miyazawa, 2009: Freakish sea state and swell-windsea coupling: Numerical study of the suwa-maru incident. *Geophysical Research Letters*, **36 (1)**, https://doi.org/https://doi.org/10.1029/2008GL036280.

Toffoli, A., J. Lefèvre, E. Bitner-Gregersen, and J. Monbaliu, 2005: Towards the identification of warning criteria: Analysis of a ship accident database. *Applied Ocean Research*, **27 (6)**, 281–291, https://doi.org/10.1016/j.apor.2006.03.003.

Accepted for publication in *Journal of Physical Oceanography*. DOI 10.1175/JPO-D-24-0251.1.

van Vledder, G. P., and L. H. Holthuijsen, 1993: The directional response of ocean waves to turning winds. *Journal of Physical Oceanography*, **23 (2)**, 177 – 192, https://doi.org/10.1175/1520-0485(1993)023⟨0177:TDROOW⟩2.0.CO;2.

Walsh, E. J., D. W. Hancock, D. E. Hines, R. N. Swift, and J. F. Scott, 1989: An observation of the directional wave spectrum evolution from shoreline to fully developed. *Journal of Physical Oceanography*, **19 (5)**, 670 – 690.

Wang, R., and H. H. Shen, 2010: Gravity waves propagating into an ice-covered ocean: A viscoelastic model. *Journal of Geophysical Research: Oceans*, **115 (C6)**, https://doi.org/10.1029/2009JC005591.

Wessel, P., and W. H. F. Smith, 1996: A global, self-consistent, hierarchical, high-resolution shoreline database. *Journal of Geophysical Research: Solid Earth*, **101 (B4)**, 8741–8743, https://doi.org/10.1029/96JB00104.

WW3DG, 2019: User Manual and System Documentation of WAVEWATCH III version 6.07, The WAVEWATCH III Development Group.

Young, I. R., S. Hasselmann, and K. Hasselmann, 1987: Computations of the response of a wave spectrum to a sudden change in wind direction. *Journal of Physical Oceanography*, **17 (9)**, 1317 – 1338, https://doi.org/10.1175/1520-0485(1987)017⟨1317:COTROA⟩2.0.CO;2.

Young, I. R., and G. P. Van Vledder, 1993: A review of the central role of nonlinear interactions in wind—wave evolution. *Philosophical Transactions of the Royal Society of London. Series A: Physical and Engineering Sciences*, **342 (1666)**, 505–524, https://doi.org/10.1098/rsta.1993.0030.

Zieger, S., A. V. Babanin, W. E. Rogers, and I. R. Young, 2015: Observation-based source terms in the third-generation wave model WAVEWATCH. *Ocean Modelling*, **96**, 2 – 25, https://doi.org/10.1016/j.ocemod.2015.07.014.

Accepted for publication in *Journal of Physical Oceanography*. DOI 10.1175/JPO-D-24-0251.1.